Evidence of distinct nonpolar/polar ordering at long/short ranges in relaxor ferroelectrics

Anuvrat Tripathi, Sanjit Ghose, Rudolph Erasmus, and Saurabh Tripathi

Phys. Rev. B **111**, 024104 — Published 9 January 2025

DOI: 10.1103/PhysRevB.111.024104

Evidence of distinct ordering (nonpolar/polar) at long/short ranges in relaxors

Anuvrat Tripathi,[1] Sanjit Ghose,[2] Rudolph Erasmus,[3] and Saurabh Tripathi[1,*]

[1]*Department of Physics, Indian Institute of Technology (BHU), Varanasi, 221005, India*
[2]*National Synchrotron Light Source II, Brookhaven National Laboratory, Upton, New York 11973, USA*
[3]*Materials for Energy Research Group, Material Physics Research Institute, School of Physics, University of the Witwatersrand, Johannesburg 2000, South Africa*

Distinct atomic ordering (non-polar/polar) has been determined at long/intermediate/short ranges using Synchrotron X-ray diffraction (SXRD), Raman scattering, and Pair Distribution Function (PDF) data in a $K_{0.5}Na_{0.5}NbO_3$ (KNN50) doped $BaTiO_3$ based relaxor ferroelectrics *viz.*, (1-*x*)$Ba_{0.9}Sr_{0.1}TiO_3$-*x*KNN50 (BKST*x*). Two different polar phases with distinct symmetries has been identified at short/intermediate-ranges for $x = 0.10$ where a monoclinic phase at short-ranges gradually transforms into a rhombohedral phase at intermediate-ranges. On the contrary, a non-polar phase with average cubic symmetry is found to be stable at long-ranges for a wide temperature range (100 K $\leq$ T $\leq$ 500 K). The polar behaviour of short/intermediate-range ordering has been quantified in terms of the amplitude of ferroelectric phonon mode Γ_4^- (q = 0,0,0) (which corresponds to the zone center of the cubic Brillouin zone). The amplitude of Γ_4^- phonon mode increases with decreasing temperature, suggesting the enhancement of ferroelectric polarisation at short/intermediate ranges on lowering temperatures. Enhanced ferroelectric polarisation at low temperature are also visible/evident by ferroelectrostriction and is quantified by the increase in magnitude of Spontaneous Volume Ferroelectrostriction (SVFS). Consequently, Zero Thermal Expansion (ZTE) is observed at low temperatures.

I. INTRODUCTION

Various properties of perovskite-based smart materials can be tailored by engineering atomic ordering at various length scales. Among perovskite-based smart materials, relaxor ferroelectrics (or relaxors) are widely studied for their numerous applications *viz.*, electrical energy storage systems, sensors & actuators, medical ultrasonic imaging, and many more [1, 2]. The relaxors possess distinct structures at long- and short ranges, responsible for various fascinating properties. Unlike ordered systems, relaxor ferroelectrics such as $PbMg_{1/3}Nb_{2/3}O_3$ (PMN) [3], $PbSc_{1/2}Ta_{1/2}O_3$ [4], $PbZn_{1/3}Nb_{2/3}O_3$ (PZN) [5], etc., exhibit chemical heterogeneity that leads to disorder resulting in enhanced physical responses [1, 2]. The relaxor behavior is often linked with the presence of polar nano regions (PNRs), which nucleate and start growing below the Burns temperature (T_B) [1, 6, 7]. The presence of PNRs and their interactions are held responsible for various physical properties observed in the relaxor material [1, 8].

Among various intriguing properties exhibited by perovskite-based oxides, controlled thermal expansion/Negative Thermal Expansion (NTE) is scientifically and technologically important [9–12]. NTE/ZTE in perovskite-based ferroelectrics is attributed to ferroelectrostriction, which is driven by large ferroelectric displacements resulting from the strong covalent nature of the A/B – O bonds [13–18]. Ferroelectrostriction in perovskite-based relaxor ferroelectrics arises from the enhanced correlations among intra/inter-polar clusters (PNRs) exhibiting ferroelectric (or polar) distortions [8, 19]. The ferroelectric (or polar) distortions responsible for ferroelectrostriction are associated with the freezing of a soft phonon mode corresponding to the zone center of the cubic Brillouin zone ($q = 0,0,0$) [20–22]. Among various phonon modes corresponding to the Γ-point of the cubic Brillouin zone, a triply degenerate Γ_4^- phonon mode (often known as ferroelectric mode) is responsible for ferroelectric (or polar) ordering. The freezing of Γ_4^- phonon mode along various dimensions leads to various low symmetry phases of $BaTiO_3$ *viz.*, *P*4*mm*, *Amm*2, and *R*3*m* with (a,0,0), (a,a,0), and (a,a,a) order parameter direction (OPD) respectively. Hence, the frozen phonon mode approach (or symmetry mode analysis) can be used to quantify the ferroelectric (or polar) distortions. [20–22]. Most of the prominent relaxor ferroelectrics are Pb-based *viz.*, PZN [9], PMN [12] etc. Due to the harmful effects of Pb on the environment and humans, various alternatives *viz.*, $Ba(Zr,Ti)O_3$ [23], $Ba(Sn,Ti)O_3$[24], $(K,Na)NbO_3$[25], $(K,Na,Ba,Sr)(Nb,Ti)O_3$[26–28] and other related materials are widely studied.

The alkali niobate-based system *viz.*, $K_{0.5}Na_{0.5}NbO_3$ (KNN50) is widely studied for its enhanced physical responses which is due to the presence of morphotropic phase boundary (MPB) [21, 25, 29–32]. Orayech et al. reported a series of structural phase transitions *viz.*, *R*3*c* $\xrightarrow{\approx 135K}$ *Amm*2 $\xrightarrow{\approx 465K}$ *P*4*mm* $\xrightarrow{\approx 700K}$ $Pm\bar{3}m$ as a function of temperature using X-ray and neutron diffraction data [21]. Moreover, later Kong et al. reported another series of phase transitions *viz.*, *Pm* $\xrightarrow{\approx 471K}$ *P*4*mm* $\xrightarrow{\approx 674K}$ $Pm\bar{3}m$, where a monoclinic phase is found to be stable down to the lowest studied temperature [25]. Further, Gupta et al. and Kong at al. confirmed the monoclinic symmetry at short ranges using Pair Distribution Function (PDF) data [25, 33].

Moreover, the alkaline earth metal-based perovskite *viz.*, $BaTiO_3$ and its solid solutions are also widely studied as a potential alternative to Pb-based materials. The doping of elements like Strontium at the A-site induces disorder/relaxor behavior in the material. Among, various compostions of Sr-doped $BaTiO_3$ *viz.*, $Ba_{(1-x)}Sr_xTiO_3$, the maximum dielectric response at ambient conditions is observed for x = 0.10

* stripathi.phy@itbhu.ac.in

(BST10). BST10 undergoes similar structural phase transitions to that of $BaTiO_3$ *i.e.*, $R3m \rightarrow Amm2 \rightarrow P4mm \rightarrow Pm\bar{3}m$ but with a shift in T_C ($\approx$ 369 K) to lower temperatures [34–38]. Among other Pb-free alternatives, KNN50 doped $BaTiO_3$ (KBTx) has been studied for its unique structural properties at short and long ranges, leading to the discovery of morphotropic relaxor boundary (MRB) [28]. Moreover, authors have doped Strontium (Sr) at the A-site of KBTx to enhance the disorder/relaxor property of the ceramics [26, 27].

In the present work, we have chosen Pb-free Sr-doped $BaTiO_3$ *viz.*, $Ba_{0.9}Sr_{0.1}TiO_3$ (BST10) as one of the parent due to its maximum dielectric response [34–37] and KNN50 as the other parent to form a solid solution *viz.*, (1-x)BST10-xKNN50 (BKSTx). The crystal structures at long ranges, along with various electrical properties, has been determined for BKSTx (x = 0, 0.05, 0.10) ceramics. A relaxor behavior is observed for x = 0.10 (BKST10) in temperature-dependent dielectric data. Moreover, the atomic ordering at various length scales (long/intermediate/short) for BKST10 has been determined using temperature-dependent Synchrotron X-ray diffraction, Raman scattering, and pair distribution function data. The ferroelectric displacements at various length scales have been quantified by calculating the amplitude of structural distortion modes using ISODISTORT. In addition, spontaneous volume ferroelectrostriction (SVFS) was calculated using the Debye-Grüniesen equation.

II. EXPERIMENTAL PROCEDURE

The BKSTx (x = 0.00, 0.05, and 0.10) ceramics were prepared using solid-state reaction technique. The precursors *viz.*, K_2CO_3 (Sisco Research Laboratories Pvt. Ltd.) (99%), Na_2CO_3 (HIMIDEA Labs) (99.5%), $BaCO_3$ (HIMIDEA Labs) (99%), $SrCO_3$ (HIMIDEA Labs) (99%), Nb_2O_5 (HIMIDEA Labs) (99.9%), and TiO_2 (HIMIDEA Labs) (99%) were pre-heated in an oven at 393 K. The heated powders were weighed as per stoichiometry and mixed *via* milling for 24 hours. After milling, the powder slurry was dried and calcined at 1173 K - 1223 K for 4 hours. The pellets were formed at 8-10 metric tons pressure and sintered at 1423 K - 1473 K for 3 hours. The room temperature X-ray diffraction data has been collected over the 2θ range 20° - 120° with a step size of 0.02, from Rigaku Miniflex 600 X-ray diffractometer having Cu-K_α radiation. The sintered pellets were electroded with silver paste on both sides for the dielectric and PE loop measurements. The dielectric measurements were carried out using a Keysight LCR meter with frequency and temperature range of 1 kHz–1 MHz and 100 K $\leq$ T $\leq$ 650 K, respectively. For PE loop measurements at 10 Hz frequency, Radiant Technology's Precision LCII Ferroelectric Tester was used. The temperature-dependent Synchrotron X-ray diffraction measurements were performed at the 28-ID-2 (XPD) beamline, in the National Synchrotron Light Source-II (NSLS-II) at Brookhaven National Laboratory (BNL) with λ = 0.1821 Å for the temperature range of 100 K $\leq T \leq$ 500 K. The intermediate- and short-range crystal structure was analyzed using temperature-dependent Raman scattering and Pair Distribution Function (PDF) data. The temperature-dependent Raman spectra were obtained *via* Horiba LabRAM HR Raman spectrometer with an Olympus BX41 microscope attachment with an excitation wavelength of 514.5 nm from a Lexel Model-95 argon ion laser. The samples were placed in a Linkam THMS600 microscope stage for Raman measurements at varying temperatures. A 50x LWD objective lens (N.A. = 0.50) was used to focus the laser beam onto the samples, and the backscattered light was dispersed using a 600 lines/mm grating onto a liquid nitrogen-cooled CCD detector. Data acquisition was carried out with LabSpec v5 software. The laser power at the sample was approximately 0.4 mW, which was confirmed to ensure there were no local heating effects from the laser. The spectral range for this study was selected to span from 80 to 1900 cm^{-1}.

The PDF data was obtained from the high-energy SXRD data, which was reduced to total scattering structure function S(Q), given as follows [39, 40]:

$$S(Q) = 1 + \frac{[I^{\mathrm{coh}}(Q) - \sum c_i |f_i(Q)|^2]}{|\sum f_i(Q) c_i|^2} \tag{1}$$

where Q is defined as Q = $4\pi \sin\theta/\lambda$ and is referred as the wave vector, 2θ is the angle between incident and diffracted beams, I^{coh} corresponds to the coherent part of the diffraction data while c_i and $f_i(Q)$ are the atomic concentrations and x-ray structure factor of atomic species of i^{th} type. The S(Q) was then transformed to final Pair Distribution Function G(r) *via* Fourier transformation with Q_{max} = 23.6 $Å^{-1}$ [39, 40]:

$$G(r) = \frac{2}{\pi} \int_{Q_{\mathrm{min}}}^{Q_{\mathrm{max}}} Q[S(Q) - 1] sin(Qr) dQ \tag{2}$$

where Q_{min} = 0.65 $Å^{-1}$.

Further, the decomposition of phonon modes has been done using the ISODISTORT tool available online [41, 42].

III. RESULTS AND DISCUSSIONS

A. XRD analysis of BKSTx ceramics

The structural analysis of BKSTx (x = 0.00, 0.05, and 0.10) ceramics has been shown in the supplementary material [43]. The parent *i.e.*, x = 0.00 (BKST0) exhibits tetragonal symmetry (Space Group: $P4mm$ [$a_0^0 a_0^0 c_+^0$]), which transforms to cubic (Space Group: $Pm\bar{3}m$ [$a_0^0 a_0^0 a_0^0$]) for both x = 0.05 (BKST5) and 0.10 (BKST10) (see Figs.1-2 of the supplementary material [43]). The electrical properties of BKSTx ceramics have been discussed in the next section.

B. Dielectric and PE loops of BKSTx ceramics

The temperature-dependent dielectric measurements for all the compositions have been carried out for a wide temper-

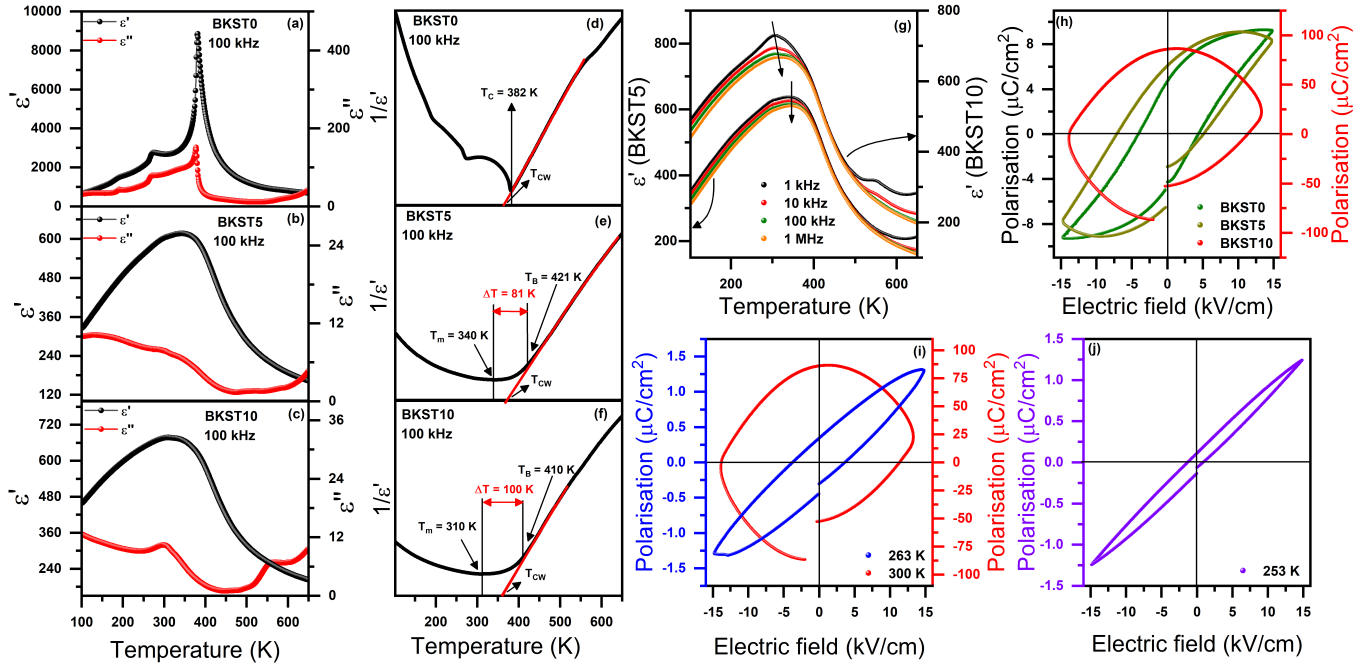

FIG. 1. Electrical properties of BKSTx ceramics including (a)-(c) The temperature-dependent real (ε') and imaginary (ε") part of BKSTx ceramics, (d)-(f) the plot between the inverse of the real part of dielectric constant with temperature *i.e.*, $1/\varepsilon$' vs. T for BKST0, BKST5, and BKST10 ceramics at 100kHz, (g) the frequency-dependent plot between real part of dielectric constant (ε') with temperature for BKST5 and BKST10 ceramics, (h) PE loops for BKSTx ceramics, and (i)-(j) temperature-dependent evolution of PE loop for BKST10 ceramics at 253 K, 263 K, and 300 K.

ature range (100 K $\leq T \leq$ 650 K). Figures 1(a)-(c) show the temperature-dependent dielectric behavior (real (ε') and imaginary (ε'') part) for BKST0, BKST5, and BKST10 ceramics at 100 kHz. For BKST0, three dielectric peaks have been observed, which are attributed to the three phase transitions *viz.*, $Pm\bar{3}m \xrightarrow{\approx 382K} P4mm \xrightarrow{\approx 274K} Amm2 \xrightarrow{\approx 192K} R3m$ similar to those of $BaTiO_3$ with a decrease in T_C [44, 45]. A single broad and diffuse dielectric peak is observed with increasing KNN50 content *i.e.*, for BKST5 and BKST10 ceramics, suggesting the presence of a diffuse phase transition. Additionally, T_m shifts towards room temperature with increasing KNN50 content (see Figs.1(d)-(f)). The normal ferroelectrics follow Curie-Weiss law above Curie temperature while the dielectric behavior of disordered ferroelectrics (exhibiting diffused dielectric peak) deviates away from Curie-Weiss law below a certain temperature referred to as Burns temperature (T_B) [1, 26, 46]. The nucleation and growth of polar nano regions (PNRs) begins below the Burns temperature [1, 2, 8]. The diffuseness of the dielectric peak can be analysed/quantified by calculating the deviation from Curie-Weiss law (ΔT_m), which is given as [26, 47]:

$$\Delta T_m = T_B - T_m \tag{3}$$

where T_B denotes Burns temperature, and T_m is the temperature corresponding to the dielectric maximum. Figures 1(d)-(f) represent the plot between the inverse of the real part of dielectric permittivity and temperature ($1/\varepsilon'$ vs. T) and depict the diffuseness (ΔT_m) of the dielectric peaks with increasing KNN50 content. For BKST0 the dielectric behavior follows the Curie-Wiess law. On the other hand, for BKST5, ΔT_m = 81 K while for BKST10, ΔT_m = 100 K, which implies an increase in the diffuseness of the dielectric peak and hence the disorder in the system with increasing KNN50 content [26], which is further supplemented by PE loops.

Figure 1(h) represents the PE loops of BKSTx ceramics. For BKST0, the loop dictates ferroelectric behavior similar to $BaTiO_3$ [48], while the shape of the loop changes with increasing KNN50 content. FE loops for BKST5 and BKST10 ceramics depict increasing disorder in the system, finally demonstrating a linear lossy dielectric behavior for BKST10 ceramics [49]. Hence, the maximum disorder is observed for BKST10 ceramics, which is further analyzed for its relaxor behavior. Figure 1(g) depicts the frequency-dependent behavior of the real part of the dielectric constant as a function of temperature. A frequency dispersion of $\Delta T \approx 6$ K has been observed in BKST10 ceramics, while BKST5 ceramics do not exhibit any frequency dispersion (see Fig.1(g)). This suggests that BKST10 is a potential relaxor, while BKST5 exhibits only a diffuse phase transition. Moreover, Figs.1(i)-(j) depicts the temperature-dependent PE loops for BKST10. It is clearly evident from the Figs.1(i)-(j) that the shape of the loop changes on lowering temperatures dictating the transformation of linear lossy dielectric to a relaxor like behavior suggesting enhancement in cationic ordering [19, 49].

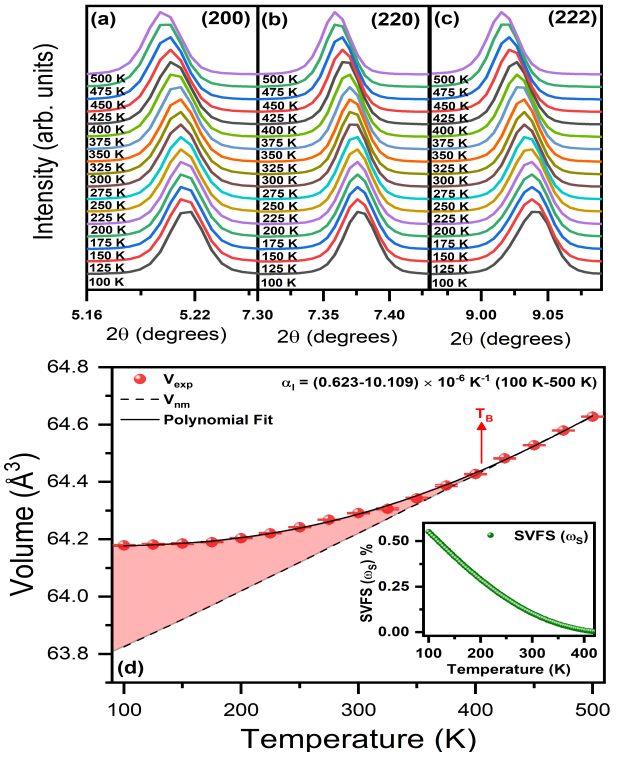

FIG. 2. (a)-(c) Temperature-dependent evolution of main perovskite peaks *viz.*, (200), (220), and (222) of BKST10 ceramics for the wide range of temperature (100 K $\leq T \leq$ 500 K), (d) Temperature-dependent evolution of volume for BKST10 ceramics. The symbols represent the experimental volume, solid and dashed lines represent the polynomial fit of experimental volume and nominal volume (V_{nm}), respectively. The inset shows the temperature-dependent evolution of Spontaneous Volume Ferroelectrostriction (SVFS) calculated using interpolated volume data.

C. SXRD analysis and zero thermal expansion in BKST10 ceramics

Owing to the relaxor behavior observed for BKST10 ceramics, the temperature-dependent evolution of the long-range crystal structure of BKST10 has been analyzed. Figure 2(a)-(c) depicts the evolution of the main perovskite peaks *viz.*, (200), (220), and (222) observed in the SXRD pattern of BKST10 ceramic for a wide temperature range (100 K $\leq T \leq$ 500 K). The peaks do not split and exhibit a singlet nature throughout the temperature range, which suggests the presence of cubic symmetry down to the lowest studied temperature. The cubic symmetry (Space Group: $Pm\bar{3}m$) is confirmed by analyzing the SXRD data using the Rietveld refinement program available at FULLPROF suite [50]. Moreover, Fig.2(d) depicts the volume as a function of temperature for BKST10 ceramics. The volume deviates from the linear behavior below the Burns temperature ($T_B \approx 410$ K), which is determined using the inverse of temperature-dependent dielectric data (see Fig.1(f)). The volume begins to saturate at low temperatures, indicating zero thermal expansion in the material.

The nearly temperature-independent volume observed at low temperatures for BKST10 ceramics suggests zero thermal expansion (ZTE) in the material (see Fig.2(d)). The ZTE is quantified using the volumetric coefficient of thermal expansion (α_V), which is defined as follows [13]:

$$\alpha_V = \frac{1}{V}\frac{\partial V}{\partial T} \tag{4}$$

where V corresponds to volume at temperature T [13, 51]. For cubic systems, the volumetric thermal expansion coefficient (α_V) is three times the linear thermal expansion coefficient (α_l), *i.e.*, $\alpha_V = 3\alpha_l$ [13]. For BKST10 ceramics, the calculated linear thermal expansion coefficient (α_l) ranges between 0.623-10.109 $\times$ 10^{-6} K^{-1} (100 K-500 K), which suggests the ZTE behavior in BKST10 ceramic [19].

As discussed earlier, the NTE/ZTE in perovskite based materials results due to ferroelectrostriction. The ferreoelctrostriction causes volume gain (or Ferroelectrovolume Effect) [12] in the material, which can be quantified using spontaneous volume ferroelectrostriction (SVFS), which is defined as follows[13, 14, 16]:

$$\omega_S = \frac{V_{exp} - V_{nm}}{V_{nm}} \times 100\% \tag{5}$$

where ω_S represents SVFS, V_{exp}, and V_{nm} correspond to experimental and nominal volume, respectively. V_{exp} is obtained from the lattice parameter after refinement, while V_{nm} is obtained after fitting the experimental volume using the Debye-Grüniesen equation in the temperature range of 400 K $\leq T \leq$ 500 K (see the supplementary material [43]) as the deviations begin near the Burns temperature ($T_B \approx 410$ K) [13, 51, 52].

Figure 2(d) depicts the ZTE behavior of BKST10 ceramics. The volume gain arising from the ferroelectrostriction can be clearly observed. The inset of the figure depicts the evolution of SVFS (ω_S) with temperature. The SVFS (or ferroelectrostriction) increases with decreasing temperatures. The increase in SVFS suggests an increase in ferroelectrostriction, consequently resulting in ZTE in the material. Furthermore, the presence of ZTE in BKST10 ceramics is attributed to the relaxor behavior of the material having distinct atomic ordering at various length scales, which will be discussed in the following sections.

D. Raman analysis of BKST10 ceramics

Owing to the relaxor behavior of BKST10 ceramics, the presence of PNRs is obvious. SXRD, Raman scattering, and Pair distribution function are the unique techniques used to analyze the symmetry of the materials at different length scales [55]. Temperature-dependent Raman spectra have been obtained to analyze the symmetry of BKST10 ceramics at intermediate ranges. Figure 3 depicts the evolution of Raman spectra at 77 K, 300 K, and 527 K. The long-range struc-

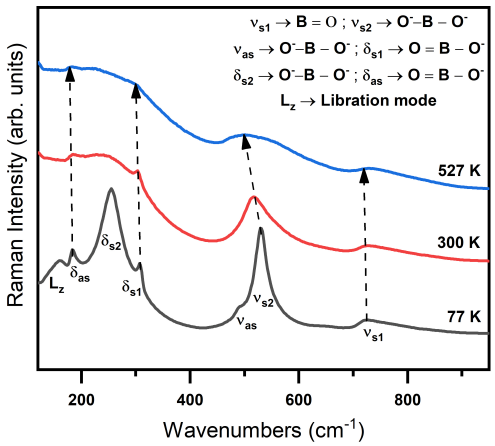

FIG. 3. The Raman spectra of BKST10 ceramic at 77 K, 300 K, and 527 K . Description of various modes have been mentioned on the top right of the figure [53, 54] also in Table VII of the supplementary material [43].

ture of BKST10 ceramics is cubic (Space Group: $Pm\bar{3}m$) with five triply degenerate phonon modes [56]. Among these, there is one triply degenerate acoustic phonon mode (T_{1u}), and the remaining four are optical phonon modes, which comprise three polar T_{1u} mode and one nonpolar T_{2u} mode *i.e.*, T_{2u} + $3T_{1u}$ [56]. All these phonon modes are Raman inactive, yet we observe Raman peaks in the spectra, which suggests the presence of local distortions (or PNRs) [56]. The observed Raman spectra of BKST10 ceramics feature seven bands (mentioned in Table VII of the supplementary material [43]) similar to the rhombohedral phase of $BaTiO_3$ [53, 54]. Among these seven bands, six correspond to the internal vibrations of BO_3^{2-} anion, while the seventh band (or lowest frequency band) corresponds to libration mode of BO_6 octahedra [53, 57]. The presence of all these bands in the Raman spectra of BKST10 confirms the rhombohedral symmetry. The six modes corresponding to internal vibrations of BO_3^{2-} are divided into two categories *viz.*, stretching modes or high-frequency modes (denoted by ν) and bending modes or low-frequency modes (denoted by δ). Both of the modes could be symmetric or asymmetric, represented by "s" or "as" respectively in the subscript [53, 54]. The presence of B=O stretching vibrations (ν_{s1} peak) around 727 cm^{-1} is clear evidence of the polar distortions in BO_6 octahedra [53]. This peak remains present in all three studied temperatures, confirming the existence of polar distortions up to the highest temperature [53, 58, 59]. Further, the symmetry of BKST10 ceramics at different length scales has been analysed/confirmed using temperature-dependent PDF data, which will be discussed in the next section.

E. PDF analysis of BKST10 ceramics

The symmetry of BKST10 ceramics at various length scales *viz.*, short and intermediate ranges can be confirmed using PDF analysis/refinements. We have determined the symmetry of BKST10 ceramics at various length scales and three different temperatures *viz.*, 100 K, 300 K, and 500 K. Figure 4 depicts the PDF fits of BKST10 ceramics at 100 K at different length scales for rhombohedral (orange line) and monoclinic (green line) symmetry. Owing to the rhombohedral symmetry concluded from Raman spectra, $R3m$ [$a_+^0 a_+^0 a_+^0$] space group was used to refine the PDF data for the range 1.7 Å $\leq$ r $\leq$ 10 Å. Various misfits were observed at different bond lengths, as indicated by the black arrow in Fig.4(a). Thereafter, PDF data was fitted using monoclinic symmetry (Space Group: Pm [$a_+^0 b_+^0 c_0^0$]) at short ranges (1.7 Å $\leq$ r $\leq$ 10 Å). Here, it is important to note that this monoclinic phase is reported for KNN50 both at long and short ranges stable for wide temperature ranges (100 K $\leq$ T $\leq$ 471 K) [25, 33]. This is reminiscent of an earlier report on $NaNbO_3$ published in Physical Review B [60]. The PDF fit significantly improves with the Pm space group and gives a lower R_w value for 1.7 Å $\leq$ r $\leq$ 10 Å in comparison to the $R3m$ space group (see Fig.4(a)), confirming a monoclinic (Pm) symmetry at short ranges (r $\leq$ 10 Å).

Moreover, at higher interatomic distances *i.e.*, for r > 10 Å (intermediate ranges), the PDF data has been fitted using the Pm and $R3m$ space groups. It is clearly observed that at intermediate ranges (r > 10 Å), the $R3m$ phase fits the PDF data better than the Pm phase, with lower R_w values obtained for the $R3m$ phase at different length scales *viz.*, 15 Å $\leq$ r $\leq$ 25 Å, 20 Å $\leq$ r $\leq$ 30 Å, and 30 Å $\leq$ r $\leq$ 40 Å (see Figs.4(c)-(e)). This analysis of PDF fits across various length scales at intermediate ranges confirms the gradual transformation from Pm to $R3m$ phase at higher length scales *i.e.*, intermediate ranges. Now, as discussed in the previous section, a rhombohedral symmetry has been confirmed at intermediate ranges at all temperatures (77 K, 300 K, and 527 K) by Raman scattering. This is further validated *via* PDF refinements at intermediate ranges, where a rhombohedral phase ($R3m$) gives a better fit relative to the Pm phase observed at short ranges (r $\leq$ 10 Å). Hence, PDF analysis at a higher length scale (intermediate ranges) conforms well with the observed Raman spectra.

Furthermore, the PDF refinements have also been done for 300K and 500K at short and intermediate ranges using monoclinic and rhombohedral phases, respectively. The refinements at short ranges (1.7 Å $\leq$ r $\leq$ 10 Å) with monoclinic (Pm) and rhombohedral ($R3m$) space groups at 100 K, 300 K, and 500 K are shown in Fig.5 of the supplementary material [43]. The monoclinic symmetry provides better fits (with lower R_w values) for r $\leq$ 10 at all the temperatures (see Fig.5 of the supplementary material [43]), confirming monoclinic phase (Pm) at short ranges for a wide temperature range. Moreover, the rhombohedral phase was confirmed at intermediate ranges using Raman scattering (see Fig.3) and PDF data (see Fig.6 of the supplementary material [43]) for a wide temperature range (100 K $\leq$ T $\leq$ 500 K). Further, the structural parameters obtained after PDF refinements at short and intermediate ranges (see Tables IV-VI of the supplementary material [43]) were used for symmetry mode analysis in the next section.

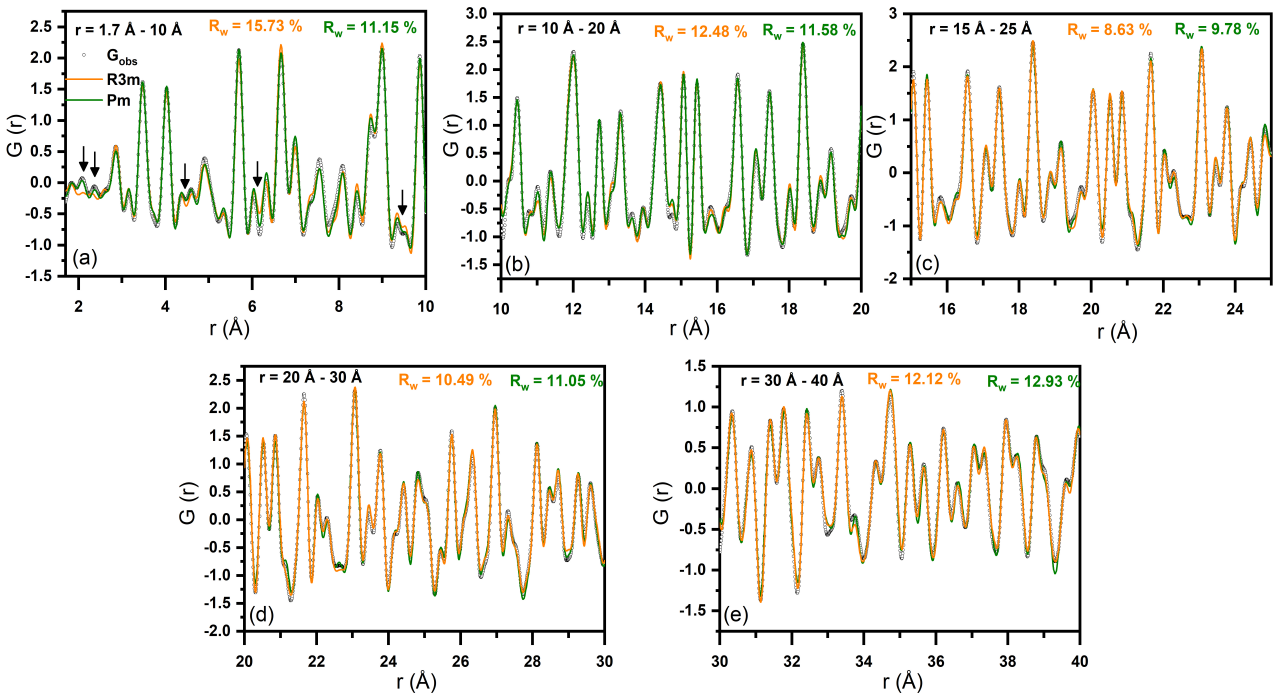

FIG. 4. The fitting of PDF profiles at various length scales *viz.*, (a) 1.7 Å- 10 Å, (b) 10 Å- 20 Å, (c) 15 Å- 25 Å, (d) 20 Å- 30 Å and, (e) 30 Å- 40 Å using *Pm* and *R*3*m* space groups, where black open circles denote observed PDF data while orange and green lines correspond to *R*3*m* and *Pm* fit respectively. The arrow represents the misfit observed by the R3m space group at r $\leq$ 10 Å.

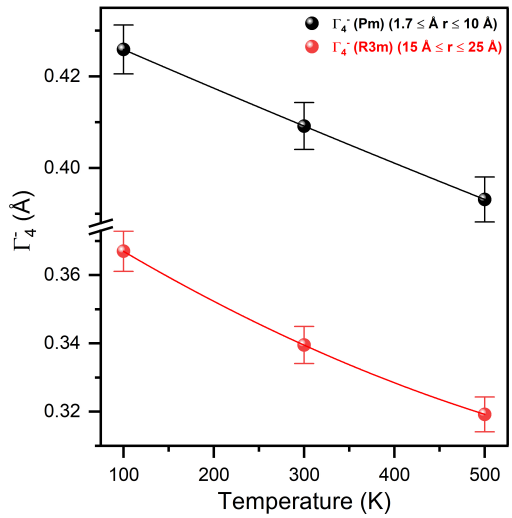

FIG. 5. Temperature-dependent evolution of the amplitude of the ferroelectric phonon mode (Γ_4^-) for Pm (1.7 Å $\leq$ r $\leq$ 10 Å), and R3m (15 Å $\leq$ r $\leq$ 25 Å) phase.

F. Frozen phonon mode approach

The static atomic displacements are held responsible for distortions within the unit cell [22, 61]. In order to quantify these distortions, the frozen phonon mode approach has been considered. The freezing of phonon mode(s) associated with the cubic Brillouin zone along certain dimensions with equal/unequal magnitudes leads to the stabilization of a low symmetry phase. The phonon mode responsible for symmetry breaking is referred to as primary, while other phonon mode(s) are referred to as secondary [22, 61, 62]. A cubic phase ($Pm\bar{3}m$ space group) with lattice parameter a = 4.00934 Å while A-site, B- site, and Oxygen atoms are fixed at 1b (0.5,0.5,0.5), 1a (0,0,0), and 3d (0.5,0,0) Wyckoff positions respectively is used as the high symmetry phase. The high symmetry phase is related to the low symmetry phase *via* a group-subgroup relation given as follows [20, 62, 63]:

$$r(\mu,i) = r_0(\mu,i) + u(\mu,i) \tag{6}$$

where r(μ, i) corresponds to the position of μ (= 1, 2, 3, 4,....) atom of low symmetry space group, $r_0(\mu, i)$ corresponds to atomic positions of high symmetry and u(μ, i) are the static displacements associated to low symmetry phase.

Now, in order to quantify the ferroelectric distortions present in the structure at short and intermediate ranges, the amplitude of symmetry adapted distortions were calculated using ISODISTORT [41, 42]. As discussed earlier, a monoclinic (*Pm*) and rhombohedral (*R*3*m*) phase is observed for short and intermediate ranges, respectively. The monoclinic and rhombohedral phase results from the freezing of the triply degenerate ferroelectric phonon mode (Γ_4^-) having Order Parameter Direction (OPD) (a,0,b) and (a,a,a), respectively.

Figure 5 depicts the variation of the amplitude of ferroelec-

tric phonon mode (Γ_4^-) as a function of temperature for a short (1.7 Å $\leq$ r $\leq$ 10 Å) and intermediate range (15 Å $\leq$ r $\leq$ 25 Å). The amplitude of the ferroelectric (FE) phonon mode quantifies the ferroelectric distortions present in PNRs. Moreover, the amplitude of FE phonon mode increases on lowering temperatures (see Fig.5). This increase in the amplitude of the FE phonon mode can be linked with an increase in the ferroelectric polarization of PNRs. Therefore, enhanced ferroelectric polarisation (amplitude of Γ_4^-) at low temperatures can be attributed to thermally induced ferroelectrostriction (volume gain), which can be considered as the origin of zeroth thermal expansion in the material.

IV. CONCLUSION

In conclusion, distinct atomic ordering (non-polar/polar) has been observed at various length scales in a ferroelectric relaxor *viz.*, 0.90(BST10)-0.10(KNN50) (BKST10) has been determined and quantified by analyzing temperature-dependent real (PDF) and reciprocal space (SXRD) data in conjunction with symmetry mode analysis. Successive ferroelectric phases *viz.*, monoclinic (*Pm*) and rhombohedral (*R*3*m*) have been identified at short- and intermediate ranges *via* integrated analysis of temperature-dependent Raman scattering and PDF data. On the contrary, a centrosymmetric non-polar cubic phase ($Pm\bar{3}m$) has been confirmed at long ranges using temperature-dependent SXRD. The ferroelectric (or polar) distortions observed at short and intermediate ranges have been quantified in terms of the amplitude of ferroelectric phonon mode Γ_4^-. The amplitude of Γ_4^- phonon mode increases with the decrease in temperatures, suggesting an increase in ferroelectric polarisation on lowering temperatures. This increase in ferroelectric polarisation at short/intermediate ranges, along with an increase in intra/inter-polar cluster interactions, has been attributed to the volume gain (ferroelectrostriction) in the material at low temperatures. Thus, ferroelectrostriction results in Zero Thermal Expansion (ZTE) with a linear coefficient of thermal expansion ranging from 0.623-10.109 $\times$ 10^{-6} K^{-1} (100 K-500 K).

V. ACKNOWLEDGMENTS

S.T. acknowledges financial assistance from the Defence Research and Development Organisation (Grant No. ERIP/ER/202210003/M/01/1812) and DST-SERB, Government of India (Grant No. CRG/2021/006000). This research used 28-ID-2 XPD beamline of the National Synchrotron Light Source II, the National Synchrotron Light Source II, a U.S. Department of Energy (DOE) Office of Science User Facility operated for the DOE Office of Science by Brookhaven National Laboratory under Contract No. DE-SC0012704.

[1] A. Bokov and Z.-G. Ye, Recent progress in relaxor ferroelectrics with perovskite structure, Journal of materials science **41**, 31 (2006).
[2] A. A. Bokov and Z.-G. Ye, Dielectric relaxation in relaxor ferroelectrics, Journal of Advanced dielectrics **2**, 1241010 (2012).
[3] G. Smolenskii and V. Isupov, Ai agranovskaya, and sn popov, Sov. Phys. Solid State **2**, 2584 (1961).
[4] F. Chu, N. Setter, and A. Tagantsev, The spontaneous relaxor-ferroelectric transition of $Pb(Sc_{0.5}Ta_{0.5})O_3$, Journal of applied physics **74**, 5129 (1993).
[5] G. A. Samara, The relaxational properties of compositionally disordered ABO_3 perovskites, Journal of Physics: Condensed Matter **15**, R367 (2003).
[6] B. Dkhil, P. Gemeiner, A. Al-Barakaty, L. Bellaiche, E. Dul'kin, E. Mojaev, and M. Roth, Intermediate temperature scale T^* in lead-based relaxor systems, Physical Review B **80**, 064103 (2009).
[7] C. W. Ahn, C.-H. Hong, B.-Y. Choi, H.-P. Kim, H.-S. Han, Y. Hwang, W. Jo, K. Wang, J.-F. Li, J.-S. Lee, *et al.*, A brief review on relaxor ferroelectrics and selected issues in lead-free relaxors, Journal of the Korean Physical Society **68**, 1481 (2016).
[8] D. N. Dubey, G. Singh, and S. Tripathi, Relaxor ferroelectricity driven by 'A'and 'B'site off-centered displacements in cubic phase with $Pm\bar{3}m$ space group, Journal of Physics D: Applied Physics **54**, 365304 (2021).
[9] J. Forrester, E. Kisi, K. Knight, and C. Howard, Rhombohedral to cubic phase transition in the relaxor ferroelectric PZN, Journal of Physics: Condensed Matter **18**, L233 (2006).
[10] S. P. Singh, D. Pandey, S. Yoon, S. Baik, and N. Shin, Evidence for monoclinic crystal structure and negative thermal expansion below magnetic transition temperature in $Pb(Fe_{1/2}Nb_{1/2})O_3$, Applied physics letters **90** (2007).
[11] T. Maiti, R. Guo, and A. Bhalla, Structure-property phase diagram of $BaZr_xTi_{1-x}O_3$ system, Journal of the American Ceramic Society **91**, 1769 (2008).
[12] J. Zhao, A. Glazounov, Q. Zhang, and B. Toby, Neutron diffraction study of electrostrictive coefficients of prototype cubic phase of relaxor ferroelectric $PbMg_{1/3}Nb_{2/3}O_3$, Applied physics letters **72**, 1048 (1998).
[13] J. Chen, L. Hu, J. Deng, and X. Xing, Negative thermal expansion in functional materials: controllable thermal expansion by chemical modifications, Chemical Society Reviews **44**, 3522 (2015).
[14] Z. Pan, J. Chen, X. Jiang, L. Hu, R. Yu, H. Yamamoto, T. Ogata, Y. Hattori, F. Guo, X. Fan, *et al.*, Colossal volume contraction in strong polar perovskites of Pb $(Ti,V)O_3$, Journal of the American Chemical Society **139**, 14865 (2017).
[15] T. Yang, Y. Wang, L. Fan, N. Wang, K. Lin, J. Chen, and X. Xing, Strong Covalent Bonding for Enhanced Negative Thermal Expansion in (1-x)$PbTiO_3$-x$BiGaO_3$, The Journal of Physical Chemistry C **124**, 20445 (2020).
[16] J. Chen, F. Wang, Q. Huang, L. Hu, X. Song, J. Deng, R. Yu, and X. Xing, Effectively control negative thermal expansion of single-phase ferroelectrics of $PbTiO_3$-(Bi, La) FeO_3 over a giant range, Scientific reports **3**, 2458 (2013).
[17] H. Yamamoto, T. Imai, Y. Sakai, and M. Azuma, Colossal negative thermal expansion in electron-doped $PbVO_3$ perovskites, Angewandte Chemie International Edition **57**, 8170 (2018).

[18] Z. Pan, X. Jiang, T. Nishikubo, Y. Sakai, H. Ishizaki, K. Oka, Z. Lin, and M. Azuma, Pronounced negative thermal expansion in lead-free $BiCoO_3$-based ferroelectrics triggered by the stabilized perovskite structure, Chemistry of Materials **31**, 6187 (2019).

[19] A. Tripathi, A. Pandey, J. A. Alonso, R. Erasmus, M. T. Fernandez-Diaz, and S. Tripathi, Origin of zero thermal expansion in an average cubic structure in Pb-free relaxor ferroelectrics, Applied Physics Letters **125**, 102901 (2024), https://pubs.aip.org/aip/apl/article-pdf/doi/10.1063/5.0219631/20139994/102901_1_5.0219631.pdf.

[20] J. Perez-Mato, D. Orobengoa, and M. Aroyo, Mode crystallography of distorted structures, Acta Crystallographica Section A: Foundations of Crystallography **66**, 558 (2010).

[21] B. Orayech, A. Faik, G. López, O. Fabelo, and J. Igartua, Mode-crystallography analysis of the crystal structures and the low-and high-temperature phase transitions in $Na_{0.5}K_{0.5}NbO_3$, Journal of Applied Crystallography **48**, 318 (2015).

[22] A. Tripathi, D. N. Dubey, H. Kumar, and S. Tripathi, Stabilizing ferroelectricity in alkaline-earth-metal-based perovskites (ABO_3) via *A*- ($Ca^2+/Sr^2+/Ba^2+$) and *B*-site (Ti^4+) cationic radius ratio (R_A/R_B), Journal of Applied Crystallography **55**, 1446 (2022).

[23] V. Buscaglia, S. Tripathi, V. Petkov, M. Dapiaggi, M. Deluca, A. Gajović, and Y. Ren, Average and local atomic-scale structure in $BaZr_xTi_{1-x}O_3$ (x= 0.10, 0.20, 0.40) ceramics by high-energy x-ray diffraction and Raman spectroscopy, Journal of Physics: Condensed Matter **26**, 065901 (2014).

[24] V. Shvartsman, J. Dec, Z. Xu, J. Banys, P. Keburis, and W. Kleemann, Crossover from ferroelectric to relaxor behavior in $BaTi_{1-x}$ Sn_xO_3 solid solutions, Phase Transitions **81**, 1013 (2008).

[25] J. Kong, J. Liu, F. Marlton, M. R. V. Jørgensen, and A. Pramanick, Local structural mechanism for phase transition and ferroelectric polarization in the mixed oxide $K_{0.5}Na_{0.5}NbO_3$, Physical Review B **103**, 184104 (2021).

[26] H. Du, W. Zhou, F. Luo, D. Zhu, S. Qu, and Z. Pei, Phase structure, dielectric properties, and relaxor behavior of $(K_{0.5}Na_{0.5})$ NbO_3-$(Ba_{0.5}Sr_{0.5})TiO_3$ lead-free solid solution for high temperature applications, Journal of Applied Physics **105** (2009).

[27] S. Sahoo, D. K. Pradhan, S. Kumari, K. S. Samantaray, C. Singh, A. Mishra, M. M. Rahaman, B. Behera, A. Kumar, R. Thomas, *et al.*, Compositional induced structural phase transitions in (1- x)$(K_{0.5}Na_{0.5})NbO_3$-x$(Ba_{0.5}Sr_{0.5})TiO_3$ ferroelectric solid solutions, Scientific Reports **13**, 19096 (2023).

[28] Y. Yang, Y. Ji, M. Fang, Z. Zhou, L. Zhang, and X. Ren, Morphotropic relaxor boundary in a relaxor system showing enhancement of electrostrain and dielectric permittivity, Physical review letters **123**, 137601 (2019).

[29] B. Jaffe, W. R. Cook, and H. Jaffe, *Piezoelectric ceramics* (Academic Press, London 1971).

[30] E. Cross, Lead-free at last, Nature **432**, 24 (2004).

[31] G. Shirane, H. Danner, A. Pavlovic, and R. Pepinsky, Phase transitions in ferroelectric $KNbO_3$, Physical Review **93**, 672 (1954).

[32] W. Ge, J. Li, D. Viehland, Y. Chang, and G. L. Messing, Electric-field-dependent phase volume fractions and enhanced piezoelectricity near the polymorphic phase boundary of $(K_{0.5}Na_{0.5})_{(1-x)}Li_xNbO_3$ textured ceramics, Physical Review B—Condensed Matter and Materials Physics **83**, 224110 (2011).

[33] S. Gupta, V. Petkov, and S. Priya, Local atomic structure of $K_xNa_{(1-x)}NbO_3$ by total x-ray diffraction, Applied Physics Letters **105** (2014).

[34] M. Kumar, A. Garg, R. Kumar, and M. Bhatnagar, Structural, dielectric and ferroelectric study of $Ba_{0.9}Sr_{0.1}Zr_xTi_{1-x}O_3$ ceramics prepared by the sol-gel method, Physica B: Condensed Matter **403**, 1819 (2008).

[35] A. Ianculescu, I. Pintilie, C. Vasilescu, M. Botea, A. Iuga, A. Melinescu, N. Drăgan, and L. Pintilie, Intrinsic pyroelectric properties of thick, coarse grained $Ba_{1-x}Sr_xTiO_3$ ceramics, Ceramics International **42**, 10338 (2016).

[36] W. Li, Z. Xu, R. Chu, P. Fu, and J. Hao, Sol–gel synthesis and characterization of $Ba_{(1-x)}Sr_xTiO_3$ ceramics, Journal of Alloys and Compounds **499**, 255 (2010).

[37] S. Gel, Effect of strontium on the structural and piezoelectric properties of the sol gel processed barium titanate, J. Mater. Environ. Sci **8**, 4945 (2017).

[38] E. K. Al-Shakarchi and N. B. Mahmood, Three techniques used to produce $BaTiO_3$ fine powder, Journal of Modern Physics **2011** (2011).

[39] V. Petkov, Pair distribution functions analysis, Characterization of Materials **1361** (2012).

[40] X. Wang, S. Tan, X.-Q. Yang, and E. Hu, Pair distribution function analysis: Fundamentals and application to battery materials, Chinese Physics B **29**, 028802 (2020).

[41] H. T. Stokes, S. v. Orden, and B. J. Campbell, Isosubgroup: an internet tool for generating isotropy subgroups of crystallographic space groups, Journal of Applied Crystallography **49**, 1849 (2016).

[42] B. J. Campbell, H. T. Stokes, D. E. Tanner, and D. M. Hatch, Isodisplace: a web-based tool for exploring structural distortions, Journal of Applied Crystallography **39**, 607 (2006).

[43] See supplementary material at [link] for the XRD analysis of BKST*x* ceramics, microstructure analysis of BKST*x* ceramics; Debye Gruniesen approximation; Description of Raman modes; PDF measurements; and Temperature-dependent PDF analysis. The supplementary material also contains Refs. [38, 50–52] .

[44] D. Garcia, R. Guo, and A. Bhalla, Growth and properties of $Ba_{0.9}Sr_{0.1}TiO_3$ single crystal fibers, Materials Letters **42**, 136 (2000).

[45] F. Jona and G. Shirane, Ferroelectric crystals, (No Title) (1962).

[46] C. J. Stringer, T. R. Shrout, and C. A. Randall, High-temperature perovskite relaxor ferroelectrics: A comparative study, Journal of Applied Physics **101** (2007).

[47] L. K. Pradhan and M. Kar, Relaxor ferroelectric oxides: Concept to applications, in *Multifunctional Ferroelectric Materials*, edited by D. R. Sahu (IntechOpen, Rijeka, 2021) Chap. 4.

[48] S. K. Upadhyay, V. R. Reddy, and N. Lakshmi, Study of (1-x)$BaTiO_3$-x$Ni_{0.5}Zn_{0.5}Fe_2O_4$ (x= 5, 10 and 15%) magnetoelectric ceramic composites, Journal of Asian Ceramic Societies **1**, 346 (2013).

[49] D. B. Migas, V. A. Turchenko, A. Rutkauskas, S. V. Trukhanov, T. I. Zubar, D. I. Tishkevich, A. V. Trukhanov, and N. V. Skorodumova, Temperature induced structural and polarization features in $BaFe_{12}O_{19}$, Journal of Materials Chemistry C **11**, 12406 (2023).

[50] J. Rodríguez-Carvajal, An introduction to the program, Laboratoire Léon Brillouin (2001).

[51] F. Sayetat, P. Fertey, and M. Kessler, An easy method for the determination of debye temperature from thermal expansion analyses, Journal of applied crystallography **31**, 121 (1998).

[52] T. Kiyama, K. Yoshimura, K. Kosuge, Y. Ikeda, and Y. Bando, Invar effect of $SrRuO_3$: Itinerant electron magnetism of Ru 4d electrons, Physical Review B **54**, R756 (1996).

[53] T. Sidorov, Structure of $BaTiO_3$ phases is studied by comparing neutron diffraction and Raman spectroscopy data, Russian

Journal of Inorganic Chemistry **56**, 1957 (2011).

[54] Y. I. Yuzyuk, Raman scattering spectra of ceramics, films, and superlattices of ferroelectric perovskites: A review, Physics of the Solid State **54**, 1026 (2012).

[55] B. Maier, B. Mihailova, C. Paulmann, J. Ihringer, M. Gospodinov, R. Stosch, B. Güttler, and U. Bismayer, Effect of local elastic strain on the structure of Pb-based relaxors: a comparative study of pure and Ba-and Bi-doped $PbSc_{0.5}Nb_{0.5}O_3$, Physical Review B **79**, 224108 (2009).

[56] I. Margaritescu, P. D. B. Mihaylova, and K. Datta, Local Structure and Dynamics of the Ferroelectric, (2016).

[57] M. Jauhari, S. Mishra, R. Mittal, and S. Chaplot, Probing of structural phase transitions in barium titanate modified sodium niobate using raman scattering, Journal of Raman Spectroscopy **50**, 1177 (2019).

[58] L. Veselinović, M. Mitrić, L. Mančić, M. Vukomanović, B. Hadžić, S. Marković, and D. Uskoković, The effect of Sn for Ti substitution on the average and local crystal structure of $BaTi_{1-x}Sn_xO_3$ ($0 \leq x \leq 0.20$), Journal of Applied Crystallography **47**, 999 (2014).

[59] I. Margaritescu, K. Datta, J. Chen, and B. Mihailova, Distinct temperature behavior of the local structure of (1-x)$PbTiO_3$-x$BiNi_{0.5}Ti_{0.5}O_3$ at the morphotropic phase boundary, Journal of Raman Spectroscopy **51**, 1200 (2020).

[60] L. Jiang, D. Mitchell, W. Dmowski, and T. Egami, Local structure of $NaNbO_3$: a neutron scattering study, Physical Review B **88**, 014105 (2013).

[61] W. Cochran, Crystal stability and the theory of ferroelectricity, Physical Review Letters **3**, 412 (1959).

[62] D. Orobengoa, C. Capillas, M. I. Aroyo, and J. M. Perez-Mato, Amplimodes: symmetry-mode analysis on the bilbao crystallographic server, Journal of Applied Crystallography **42**, 820 (2009).

[63] H. Kumar, A. Singh, J. L. Martinez, J. A. Alonso, and S. Tripathi, Unexplored signatures of magnetoelastic and isosymmetric metal-insulator phase transition in a rare-earth nickelate via mode crystallography, Physical Review B **106**, 214103 (2022).